Chemical Engineering Journal 156 (2010) 446–458

Contents lists available at ScienceDirect

Chemical Engineering Journal

journal homepage: www.elsevier.com/locate/cej

Interactions of phase equilibria, jet fluid dynamics and mass transfer during supercritical antisolvent micronization

E. Reverchon[a,*], E. Torino[a], S. Dowy[b], A. Braeuer[b], A. Leipertz[b]

[a] Chemical and Food Engineering Department, University of Salerno, Via Ponte Don Melillo 1, 84084 Fisciano, Salerno, Italy
[b] Lehrstuhl für Technische Thermodynamik, Erlangen Graduate School in Advanced Optical Technologies (SAOT), Universität Erlangen-Nürnberg, Am Weichselgarten 8, 91058 Erlangen, Germany

ARTICLE INFO

Article history:
Received 24 July 2009
Received in revised form 20 October 2009
Accepted 23 October 2009

Keywords:
Supercritical antisolvent process
Elastic light scattering
Phase behavior
Mixing behavior
Particle nucleation
Micronization

ABSTRACT

Supercritical antisolvent (SAS) precipitation has been successfully used in the micronization of several compounds. Nevertheless, the role of high-pressure vapor–liquid equilibria, jet fluid dynamics and mass transfer in determining particle size and morphology is still debated. In this work, CO_2 has been adopted as supercritical antisolvent and elastic light has been used to acquire information on jet fluid dynamics using thin wall injectors for the investigation of the liquid solvents acetone and DMSO at operating conditions of 40 °C in the pressure range between 6 and 16 MPa. The results show that two-phase mixing after jet break-up is the phenomenon that characterizes the jet fluid dynamics at subcritical conditions. When SAS is performed at supercritical conditions a transition between multi-phase and single-phase mixing is observed by increasing the operating pressure. Single-phase mixing is due to the very fast disappearance of the interfacial tension between the liquid solvent and the fluid phase in the precipitator. The transition between these two phenomena depends on the operating pressure, but also on the viscosity and the surface tension of the solvent. Indeed, single-phase mixing has been observed for acetone very near the mixture critical point, whereas DMSO showed a progressive transition for pressures of about 12 MPa.

In the second part of the work, a solute was added to DMSO to study the morphology of the microparticles formed during SAS precipitation at the different process conditions, to find a correlation between particle morphology and the observed jet. Expanded microparticles were obtained working at subcritical conditions; whereas spherical microparticles were obtained operating at supercritical conditions up to the pressure where the transition between multi- and single-phase mixing was observed. Nanoparticles were obtained operating far above the mixture critical pressure. The observed particle morphologies have been explained considering the interplay among high-pressure phase equilibria, fluid dynamics and mass transfer during the precipitation process.

1. Introduction

Supercritical antisolvent (SAS) micronization has been largely studied because of its wide potential of producing micrometric and nanometric particles with controlled particle size and morphology [1,2] that can be applied in several industrial fields. The process is commonly performed at temperatures ranging between 35 and 60 °C. Therefore, it is particularly useful when thermo-labile compounds have to be micronized, as in the case of pharmaceutical, cosmetic and polymeric applications. For example, reviewing SAS characteristics, Reverchon et al. demonstrated that this process is able to produce micrometric particles in the range from 1 to 20 μm for various materials [3] and to produce nanoparticles down to a mean diameter of about 50 nm [4]. The process has also been successfully scaled to pilot and semi-industrial GMP (Good Manufacturing Practice, in pharmaceuticals applications) scales [5,6]. Nevertheless, a relatively few works have been published, aimed at the understanding of the fundamental mechanisms that control the generation of the various particle morphologies during the SAS precipitation [7–11].

The SAS process is complex, since it involves the knowledge of:

1. high-pressure phase equilibria of the binary system (solvent/antisolvent) or ternary system (solvent/antisolvent/solute);
2. jet mixing, when the liquid solution is injected in the precipitator; and
3. mass transfer to and from the injected liquid phase, which causes the supersaturation and precipitation of the solute.

* Corresponding author. Tel.: +39 089 964116; fax: +39 089 964057.
E-mail address: ereverchon@unisa.it (E. Reverchon).

1385-8947/$ – see front matter © 2009 Elsevier B.V. All rights reserved.
doi:10.1016/j.cej.2009.10.052

1.1. High-pressure phase equilibria

The ternary system formed by solvent, solute and antisolvent should in principle be taken into account. However, SAS is based on the assumption that the solute is practically not soluble in the mixture solvent–antisolvent; if this hypothesis is verified, the presence of solute can be neglected and the fluid phase system formed in the precipitator can be treated as a binary one. Therefore, the considerations about position of the process operating point can be performed on the corresponding p–x isothermal diagram and typical SAS will be operated at pressures above the binary mixture critical point (MCP).

If the presence of solute in the fluid phase formed in the precipitator cannot be neglected (for example, if it was practically not soluble in the supercritical fluid, but it has a non-negligible solubility in the mixture antisolvent plus solvent) the phase equilibria can be largely different with respect to the corresponding binary system. For example, at the same pressure, the operating point in the ternary diagram could be located at subcritical conditions or inside a biphasic region. As a consequence, different equilibrium conditions apply and different transient interfacial tensions are obtained during the precipitation.

The influence of phase equilibria and of their possible modifications, due to the presence of solutes, on particle formation and morphologies has been reported by Reverchon et al. [3,4,12]. These authors tried to describe the different mechanisms involved in the SAS formation of nanoparticles, microparticles and expanded microparticles and to describe the switching between the various morphologies based on the literature data and on specifically performed experiments. Other authors used similar observations as a reference to obtain selected lysozyme particle morphologies [13].

1.2. Jet mixing

In the SAS related literature there is a general agreement about the flow regimes observable when a liquid is injected in a vessel, which is filled with the supercritical antisolvent. Lengsfeld et al. [11] has been the first group that investigated fluid dynamics of the SAS process. They studied the evolution and disappearance of the liquid surface tension of immiscible, poorly miscible and miscible fluids injected in supercritical (sc)-CO_2, to determine whether the liquid atomizes into droplets or evolves as a gaseous jet. They concluded that in the case of miscible fluids (i.e., at supercritical conditions), the surface tension vanishes before an appreciable jet break-up is obtained. Consequently, a gas-like jet is formed after the jet break-up.

Sarkari et al. [14], Badens et al. [7], Gokhale et al. [10] and Obrzut et al. [15] also concluded that turbulent single-phase mixing dominates at well developed supercritical conditions. However, the transition between multi-phase (formation of droplets after jet break-up) and single-phase mixing (no formation of droplets after jet break-up) could not be located at the pressure of the mixture critical point. Dukhin et al. [16] and Gokhale et al. [10] found that jet break-up into droplets still takes place at pressures slightly above the MCP. Particularly, Gokhale et al. [10] observed at these conditions the formation of small droplets that rapidly dissolve in sc-CO_2. Due to the non-equilibrium conditions during mixing, a dynamic (transient) interfacial tension exists that decreases between the inlet of the liquid and its transformation to a gas-like mixture.

Some authors attempted to connect the observed flow or mixing regimes to the morphology of the precipitated particles. Lee et al. [17] injected a solution of dichloromethane (DCM) and PLA at subcritical conditions in the dripping and in the Rayleigh disintegration regimes and observed the formation of uniform PLA microparticles. Other authors [10,15] did not find relevant differences in the various precipitates obtained, perhaps, as a result of using a polymer (PLA and PVP, respectively) as the solute. As a rule, polymers show a rather limited variety of precipitate morphologies in the SAS literature. Particularly, PLA morphologies showed to be insensitive to the SAS processing conditions [18,19]. This characteristic could be assigned to the high molecular weights and to the large modifications of the solution properties induced by the presence of a polymer. Moreover, polymers tend to form aggregated particles because of the reduction of the glass transition temperature in sc-CO_2.

In all the studies commented until now, jet characteristics were studied using shadowgraphic techniques. Shadowgraphy is an optical method to obtain information on non-uniformities in transparent media, independently if they arise by temperature, density or concentration gradients. All of these inhomogeneities refract light which causes shadows.

It is important to mention that light scattering experiments give insight about jet mixing, which cannot be gained by applying techniques like shadowgraphy. Especially considering atomized sprays (very droplet laden sprays) and dense jets (gas-plumes), shadowgraphy cannot differentiate between them. This is due to the fact that both the droplet laden spray and the dense "gas-plume" result in a dark shadow. On the contrary, using a light scattering technique, it is possible to clearly differentiate between an atomized very droplet laden spray and a dense "gas-plume".

1.3. Mass transfer

When droplets are formed, as a result of the jet break-up, mass transport of CO_2 into the droplet and solvent evaporation into the bulk sc-CO_2 are the two phenomena that characterize the SAS process. The mass transfer of sc-CO_2 inside the droplets is particularly fast, since CO_2 is highly soluble in organic solvents and shows gas-like diffusion properties that are characteristic for supercritical fluids.

The modeling works of Werling and Debenedetti [20,21] illustrated the mass transfer inside and outside a toluene spherical droplet below and above the MCP of the system toluene/CO_2. Convective mass transfer inside and outside the spherical fluid element was not considered during their investigations. Particularly, at subcritical conditions they predicted the rapid expansion of the droplet. Chavez et al. [22] also showed that the precipitation process confined in the droplet can occur according to two different mechanisms. The first is a diffusion limited regime that produces a precipitation front and the second is a nucleation-limited regime in a homogeneously mixed droplet. These mechanisms can influence the micro–nano-structure of the precipitated particles, especially considering that the nucleation process is simultaneously promoted in many parts inside the droplet [9] and can produce fine aggregates of nanoparticles.

Although the action of the single mechanisms has been elucidated, the potential superposition of the various mechanisms indicates that the overall process could be successfully described only, if the interactions among phase equilibria, fluid dynamics and mass transfer are taken into account all together. These mechanisms concur to the production of the precipitates and hence are responsible for the great variety of particle morphologies and sizes obtainable by SAS precipitation.

The role of mass transfer mechanisms seems to be relatively well demonstrated even if the limitation of non-considering convection inside and outside the droplets can be relevant. The contribution of phase equilibria and particularly of the SAS operating point (pressure, temperature and overall composition) has been stressed by some authors. What is generally missing is the connection between jet fluid dynamics, phase equilibria and mass transfer on the morphology and the dimensions of the generated particles.

Therefore, this work is aimed at a further elucidation of the interactions of the phase equilibria, the jet fluid dynamics, the mass transfer and the characteristics of the generated particles. For the first time, jet characteristics during SAS precipitation are studied using elastic light scattering. This technique allows distinguishing between liquid–gas phase boundaries and the formation of a gas-like jet without phase boundaries.

Systematic experiments were carried out at different operating conditions, using two solvents (acetone and dimethylsulfoxide (DMSO)) and two injection nozzles (80 and 160 μm diameter). Beyond the investigation of the pure solvents, experiments were performed with the addition of a solute (yttrium acetate (YAc)) to the liquid solvent with the aim of coupling the morphology of the precipitates to the observed jet characteristics.

2. Materials and procedures

2.1. Materials

Yttrium acetate (YAc, purity of 99.9%), dimethylsulfoxide (DMSO, purity 99.5%) and acetone (Ac, purity 99.8) were supplied by Sigma–Aldrich (Italy). Carbon dioxide (CO_2, purity 99%) was purchased from SON (Italy). All the products were used as received.

2.2. SAS experimental setup

Fig. 1 shows a sketch of the SAS laboratory plant that was used for the experiments described in this work. A HPLC pump (Gilson, mod. 305) equipped with a pulse dampener (Gilson, mod. 805) was used to deliver the liquid solution. A diaphragm high-pressure pump (Milton Roy, mod. Milroyal B) was used to deliver the CO_2. A cylindrical vessel with an inner volume of 375 cm^3 was used as precipitator. The precipitator was equipped with two quartz windows oriented line of sight. The liquid mixture was delivered to the precipitator through thin wall injectors with nozzle diameters of 80 and 160 μm, respectively. A second collection chamber located downstream the precipitator and operated at about 0.2 MPa, was used to recover the liquid solvent. Further information on the SAS plant is given elsewhere [23].

2.3. SAS procedure

A SAS experiment begins delivering sc-CO_2 to the precipitation chamber until the desired pressure is reached. When antisolvent steady flow is established, pure solvent is sent through the nozzle to the chamber for at least 15 min. When a quasi-steady state composition of solvent and antisolvent is realized within the precipitator, the flow of the pure solvent is stopped and the liquid solution is delivered through the nozzle for at least 20 min, producing the precipitation of the solute. At the end of the liquid solution delivery, the chamber is purged with supercritical CO_2 to wash it from the residual solvent solubilized in the supercritical antisolvent for at least 90 min. If the final purge with pure CO_2 is not performed, the solvent contained in the fluid phase will condense during the depressurization and will solubilize or modify the precipitates. More details about this procedure are given elsewhere [23].

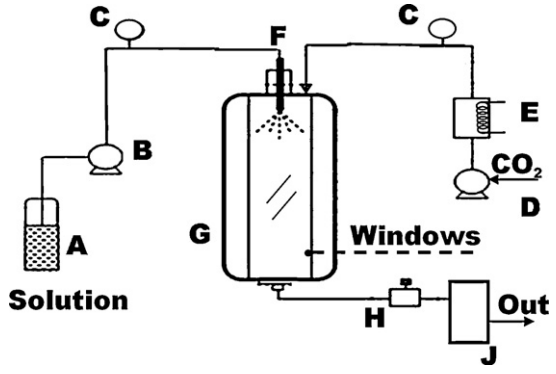

Fig. 1. SAS windowed apparatus: solution vessel (A); liquid pump (B); pressure gauge (C); CO_2 pump (D); heat exchanger (E); injection system (F); precipitator (G); pressure reducing valve (H); separator (J).

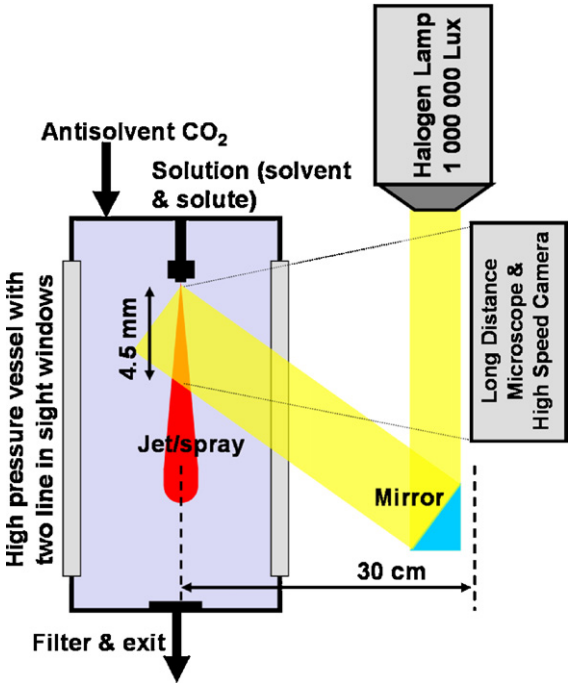

Fig. 2. Schematics of the optical setup.

2.4. SEM analysis

Samples of the precipitated powder were collected at different points inside the precipitation chamber and examined using a scanning electron microscope (SEM) (Assing, mod. LEO 420). SEM samples were covered with 250 A of gold using a sputter coater (Agar, mod. 108A). Particle size (PS) and particle size distributions (PSDs) were measured using an image processing software (Sigma Scan Pro, Jandel Scientific) that counts, measures and analyzes digital images. About 200–300 particles, coming from different images, were considered for each PSD calculation.

2.5. Light scattering setup

Fig. 2 shows a schematic of the optical setup, which was used to characterize the fluid dynamics of the injected liquid. A high power halogen lamp with 1 Mlux was used to illuminate the jet. Elastic light scattered in backward direction was collected using a long distance microscope and detected with a high speed camera. Though the long distance microscope was 30 cm away from the jet axis, 4.5 mm × 4.5 mm of the jet plane was imaged onto the 1024 × 1024 pixels of the high speed camera CMOS chip. The camera was operated with a recording rate of 5 kHz. To freeze the motion of the jet during the acquisition of one image, the exposure time of the camera was adjusted between 100 and 50 μs, depending on the propagation velocity of the jet.

Elastic light scattering means that the wavelength of the scattered light is equal to the incident wavelength. There are nine

different elastic light scattering mechanisms that are strongly related to the dimensions of the matter from which the light is scattered away from its original path and on the wavelength of the incident light, e.g., Rayleigh-, Mie- and optical scattering. In this manuscript light scattering from phase boundaries is termed Mie scattering (irrespective of the phase boundaries dimension) and light scattering from inhomogeneities is termed Rayleigh scattering. Light can be scattered away from its incident path if it interacts with a phase boundary, with inhomogeneities, or with matter in general. Refractive index inhomogeneities are caused by composition and density inhomogeneities. Pronounced density changes due to composition changes are known especially for the mixtures of CO_2 and organic solvents [8,24–26]. Consequently, regarding the mechanisms taking place in the SAS process, Mie scattering is due to the formation of a multi-phase flow; whereas Rayleigh scattering is due to composition inhomogeneities, which cause refractive index inhomogeneities.

When a pure solvent is injected into sc-CO_2, light scattering can originate from three different phenomena. Fig. 3 summarizes

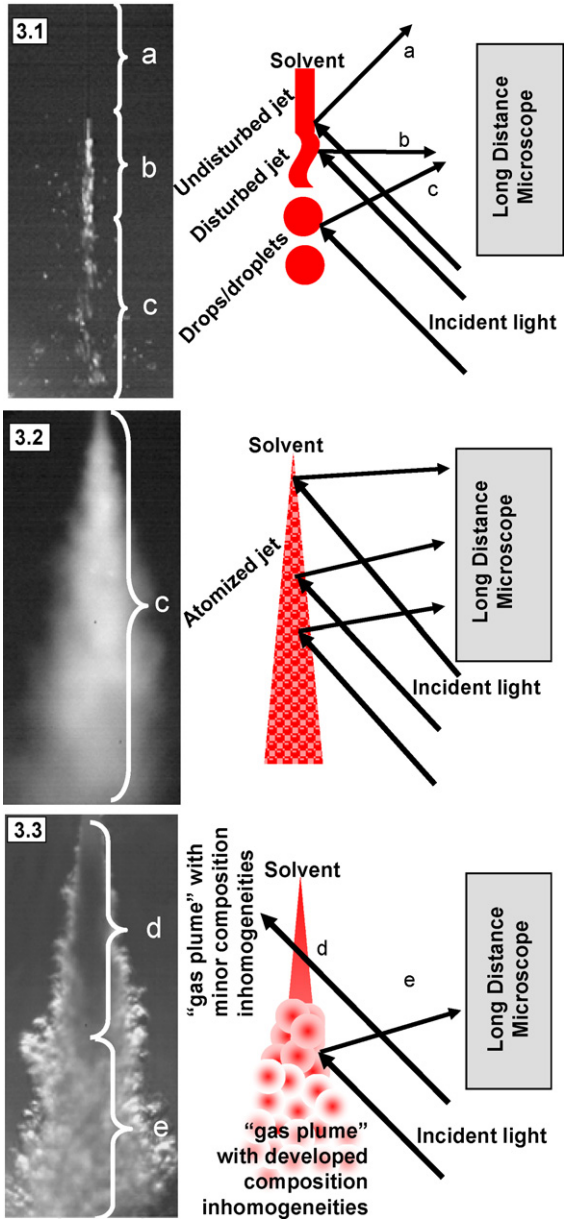

Fig. 3. Scattering phenomena related to jet mixing.

the different mixing behaviors of the injected solvent jet, observed using Mie- and Rayleigh scattering images, e.g., jet break-up into rather large droplets (drops) at a certain distance from the nozzle (Fig. 3.1), jet atomization into small droplets, which cannot be resolved by the microscope (Fig. 3.2), and "gas-plume" like mixing, when no droplets are formed (Fig. 3.3).

In Fig. 3.1 the undisturbed jet, which is indicated as part (a) is not observable, since no light is directly reflected towards the detection system. As soon as some disturbances modify the smooth surface of the homogeneous jet, the incident light is reflected towards the long distance microscope. Consequently part (b) showing the disturbed jet is observable in Fig. 3.1. Mie scattering signals from drops or droplets phase boundaries, which are formed after jet break-up, can also be detected as indicated by part (c) in Fig. 3.1. In Fig. 3.2 a jet is shown, in which atomization starts directly at the nozzle exit. Due to atomization, small droplets are formed, which cannot be resolved by the microscope. Nevertheless the strong Mie scattering signal, generated by droplets, allows obtaining the image of the white atomized jet along all the liquid trajectories. In Fig. 3.3 jet mixing without the formation of phase boundaries is illustrated. Mixing takes place in a single phase with pronounced composition inhomogeneities. In the jet core, which is indicated by part (d), the injected solvent has not yet mixed with the bulk CO_2 and, consequently, Rayleigh scattering signals are only observable at the jet edges, where composition inhomogeneities are located. Further downstream in part (e), mixing takes place in the entire jet. Therefore, Rayleigh scattering signals become more pronounced.

3. Results

In this study, DMSO and acetone were selected as the liquid solvents since they have very different physical properties and have widely been used in the SAS literature (especially DMSO). YAc was selected as the solute, since many information on the particle characteristics produced by SAS, depending on the process conditions, are already known [2]. By precipitation from DMSO, nanoparticles, spherical microparticles, and expanded particles were previously produced [3,4,12]. Therefore, YAc is a good candidate in a study aimed at interlinking process mechanisms and particle morphologies.

3.1. *Preliminary selection of the SAS operating conditions from high-pressure phase diagrams (VLEs, DMSO/CO_2, acetone/CO_2)*

All the experiments were carried out at a precipitation temperature of 40 °C and with two different thin wall injectors of 80 and 160 μm in diameter. The molar fraction of CO_2 inside the precipitator (at steady state conditions) was fixed at $x_{CO_2} \approx 0.99$. Steady state composition in the precipitator was obtained according the SAS procedure previously illustrated. CO_2 molar fraction was selected to be sure that the SAS operating point was outside the miscibility hole between CO_2 and the organic solvent (see Figs. 4–6) It means that when the liquid flow rate was varied, also the CO_2 flow rate was modified to maintain x_{CO_2} constant. According to the pressure–composition (p–x) phase diagrams of the systems DMSO/CO_2 and acetone/CO_2, which are given in Figs. 4 and 5, respectively, the selected molar fraction corresponds to single-phase systems, irrespective of the SAS operation pressure. Consequently the SAS experiments were run at a constant CO_2 molar fraction in the single-phase region, at operation conditions ranging from below to far above the mixture critical point [27]. The respective operating points are given in Fig. 6. In the selection of the operating conditions only the binary systems were considered for two reasons. First, some of the light scattering experiments were performed in the absence of a solute. Second, it is evident

Table 1
List of solvent flow rates and the corresponding nozzle exit velocities and Reynolds numbers for DMSO and acetone, for the two analyzed nozzle diameters. The Ohnesorge number is given, too.

Flow solvent [mL min^{-1}]	Nozzle exit velocity, v [m s^{-1}]		Nozzle Reynolds number, DMSO		Nozzle Reynolds number, acetone	
	80 μm nozzle	160 μm nozzle	80 μm nozzle	160 μm nozzle	80 μm nozzle	160 μm nozzle
0.25	0.83		47		192	
0.5	1.66	0.41	93		384	192
1	3.32	0.83	186	93	767	384
1.5	4.97		279		1151	
2		1.66		186		767
2.5	8.29		465		1918	
3		2.49		279		1151
3.5	11.61		651		2685	
5		4.14		465		1918
7		5.80		651		2685
Oh			2.51E−02	1.78E−02	6.73E−03	4.76E−03

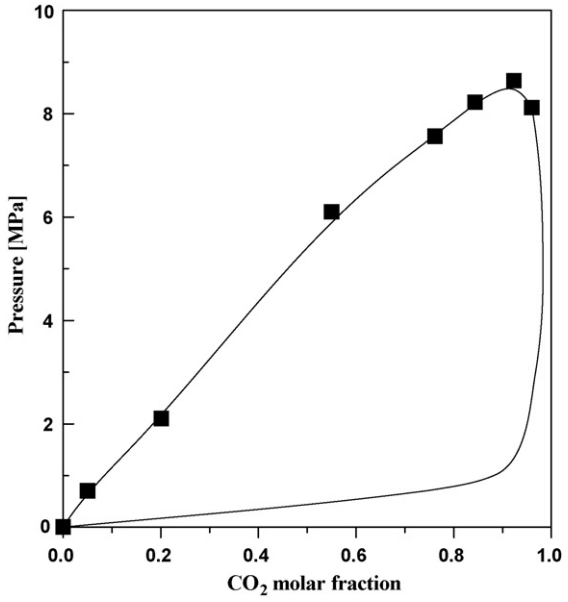

Fig. 4. Pressure–composition (p–x)-phase diagram of the binary system DMSO/CO_2 at 40 °C [28].

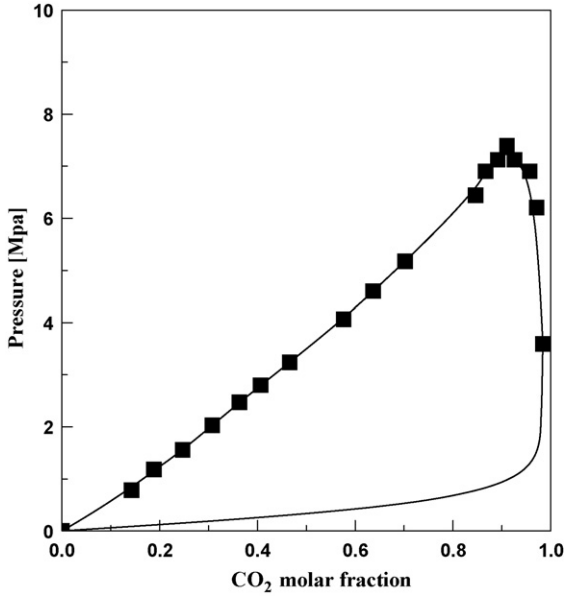

Fig. 5. Pressure–composition (p–x)-phase diagram of the binary system acetone/CO_2 at 40 °C [29].

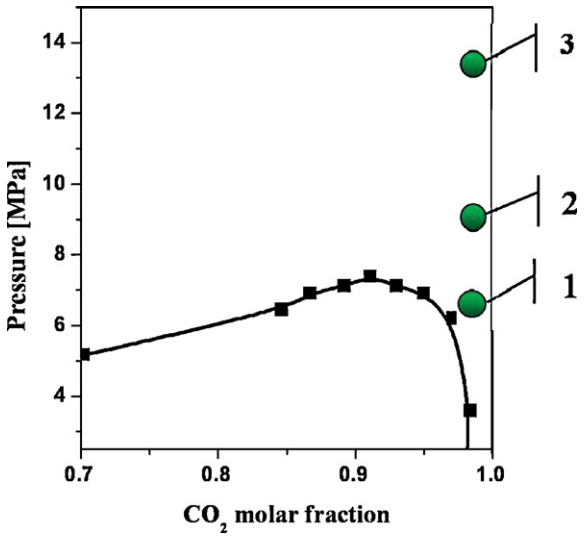

Fig. 6. Position of the operating points in the pressure–composition (p–x)-diagram of the binary system acetone/CO_2 [29].

from previous works that YAc is not soluble in the selected systems solvent/CO_2. However, if the presence of the liquid solvent induces compatibility between the solute and the sc-CO_2, modifications of the binary vapor/liquid-equilibria (VLEs) have to be taken into account. In this case the corresponding ternary diagram could, for example, show a marked dependence on the position of the MCP on the quantity (molar fraction) of solute dissolved.

Table 1 summarizes the solvent flow rates of DMSO and acetone, which were set in a pressure range from 6 to 16 MPa. The mean exit velocity in Table 1 was calculated from the solvent flow rate and the nozzle diameter, assuming plug flow. Usually, dimensionless numbers employed to describe jet fluid dynamics are the Reynolds (Re) and the Ohnesorge (Oh) number. The first one gives a measure of the ratio of inertial forces ($v\rho$) to viscous forces (μ/D), and, consequently, it quantifies the relative importance of these two types of forces for given flow conditions. The second one relates the viscous and the surface tension force by dividing the square root of Weber number by Reynolds number, which eliminates velocity from both [30]. Just to timind Weber number is defined as ($We = \rho(v_2 l/\sigma)$, where ρ is the density of the fluid, v is its velocity, l is its characteristic length (typically the droplet diameter) and σ is the surface tension.

Reynolds number and the Ohnesorge number were calculated using the following definitions:

$$\mathrm{Re} = \frac{vD\rho}{\eta} \quad (1)$$

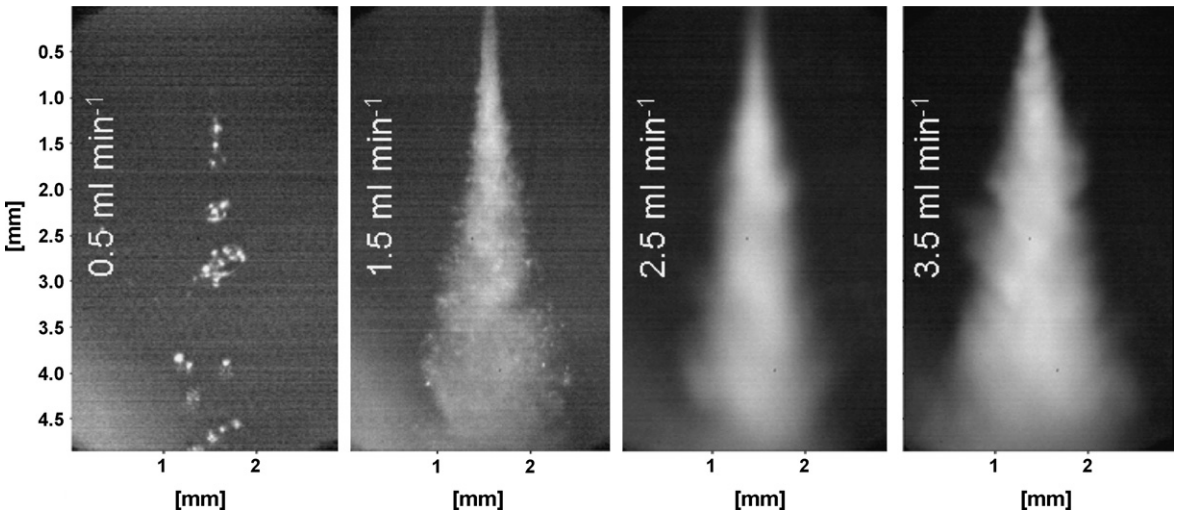

Fig. 7. Light scattering images of DMSO jet at subcritical conditions and for different flow rates (8.5 MPa, 40 °C, ⌀ = 80 μm).

Table 2
Properties of DMSO and acetone at 25 °C, required for the calculation of Re and Oh numbers; data are from Ref. [31] for (DMSO) and from the website www.fluidat.com (acetone).

Solvent	DMSO	Acetone
Density, ρ [kg m^{-3}]	1080	763.3
Dyn. viscosity, η [kg (ms)$^{-1}$]	1.5E−03	2.64E−04
Surface tension, σ [N m^{-1}]	4.35E−02	2.52E−02

$$\mathrm{Oh} = \frac{\eta}{\sqrt{D\rho\sigma}} \quad (2)$$

The properties of the two solvents are given in Table 2. The characteristic length scale D within Eqs. (1) and (2) is the injector (nozzle) diameter.

As can be extracted from Table 1, experiments were carried out using two different nozzle diameters but at the same Reynolds number values.

3.2. Subcritical conditions

Fig. 7 shows the jet behavior at subcritical conditions (8.5 MPa and 40 °C) for different flow rates of DMSO and a nozzle diameter of 80 μm. At a DMSO flow rate of 0.5 mL min^{-1} it is possible to identify parts (a), (b) and (c) of the jet in the light scattering images, as described previously in Fig. 3. The phase boundary of the invisible continuous jet, which is part (a) in Fig. 3, first becomes irregular and then breaks up into rather large drops. For the DMSO flow rate of 1.5 mL min^{-1} only part (c) is visible in the jet image. Due to the atomization of the solvent directly at the nozzle exit, droplets are formed immediately after exiting the nozzle. Single droplets are visible at 1.5 mL min^{-1} downstream of the injector nozzle. For the DMSO flow rates of 2.5 and 3.5 mL min^{-1}, single droplets are no more visible in the dense droplet laden atomized spray. Nevertheless, the intense Mie scattering signals must be assigned to a highly atomized spray, formed by small droplets.

As the pressure of 8.5 MPa exceeds the MCP for the binary system acetone/CO_2, the subcritical experiments with acetone were carried out at pressures between 6 and 7.5 MPa. Fig. 8 shows the acetone jet behavior at subcritical conditions (7.5 MPa and 40 °C) for different flow rates of acetone and the nozzle diameter of 80 μm. Dripping is observed at the lower flow rates and atomization develops at higher flow rates as in the case of DMSO. In contrast to DMSO, single drops can be identified for all analyzed acetone flow rates. This result must be assigned to the differences in the Reynolds

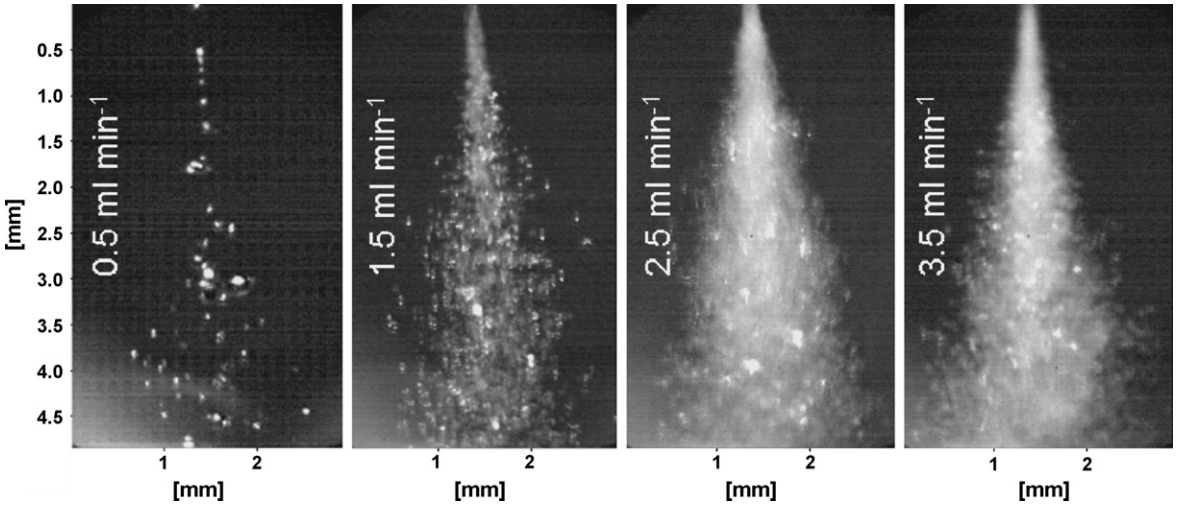

Fig. 8. Light scattering images of acetone for different flow rates at subcritical conditions (7.5 MPa, 40 °C, ⌀ = 80 μm).

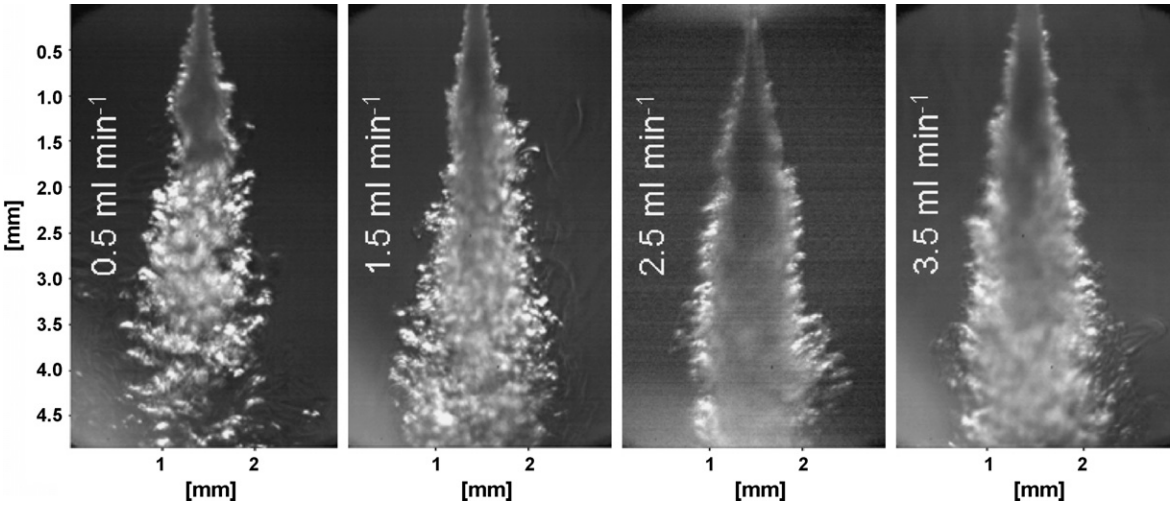

Fig. 9. Light scattering images of DMSO at fully developed supercritical conditions and for different flow rates (16 MPa, 40 °C, ∅ = 80 μm).

number, the Ohnesorge number and the pressure of the DMSO and acetone experiments (see Table 1).

3.3. Far above the MCP

Fig. 9 shows the jet behavior at fully developed supercritical conditions (16 MPa and 40 °C) for different flow rates of DMSO and the nozzle diameter of 80 μm. Irrespective of the DMSO flow rate, the light scattering images in Fig. 9 consist of part (d) and part (e), as described previously in Fig. 3. Consequently, it is possible to identify a jet core in the centre of the jet (part d), and Rayleigh scattering signals (part e) at the edges of the jet and further downstream. Increasing the DMSO flow rate, the jet core enlarges and shifts the region of pronounced composition inhomogeneities downstream. As no Mie scattering signal was observed for all analyzed DMSO flow rates, no phase boundaries can be detected. Hence, jet mixing at fully developed supercritical conditions is a single-phase mixing process.

When experiments at the same flow rates and pressures are carried out with acetone, according to Fig. 10, the general jet characteristics remain unaltered. For acetone, part (d) of the jet is much shorter than for DMSO and consequently the region of pronounced composition inhomogeneities can be observed much closer to the injection nozzle. This fact depends on the density and viscosity differences of the two solvents, which are both larger for DMSO. Consequently, for the injection of DMSO, a higher mass flow rate with lower volatility is injected when compared to acetone experiments.

3.4. Near above the MCP

Fig. 11 shows the jet behavior at conditions near above the MCP (10 MPa and 40 °C) for different flow rates of DMSO and the nozzle diameter of 80 μm. According to Fig. 4, these process conditions are near above the MCP of the binary system DMSO/CO_2. For all DMSO flow rates, bright Mie scattering signals are observable in the jet centre; whereas further downstream, gradient scattering signals can be observed. Therefore, in these cases the injected solvent is first atomized into small droplets, which is represented by part (b) in Fig. 3. With increasing DMSO flow rate, the mean nozzle exit velocity (and Re) is increased. Consequently, the jet break-up length is shortened. Both, the shortened jet break-up length in combination with the increased nozzle exit velocity, decrease the residence time of a fluid element between the nozzle exit and the jet break-up. If the time required for the complete degradation of the transient interfacial tension between the injected solvent and the bulk CO_2 is less than the residence time before jet break-up, no droplets are formed after jet break-up. If the time required for the

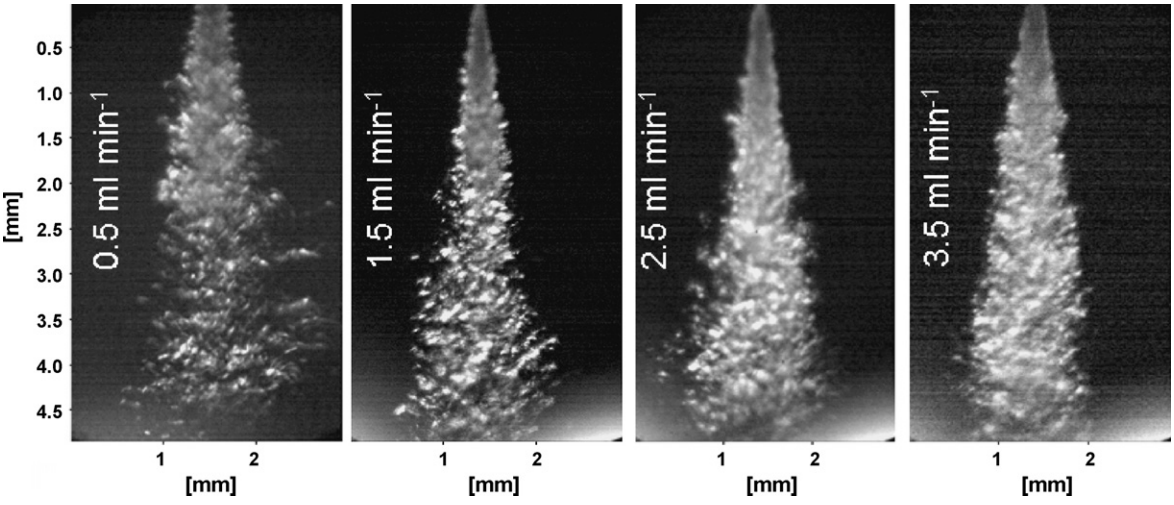

Fig. 10. Light scattering images of acetone at fully developed supercritical conditions and for different flow rates (16 MPa, 40 °C, ∅ = 80 μm).

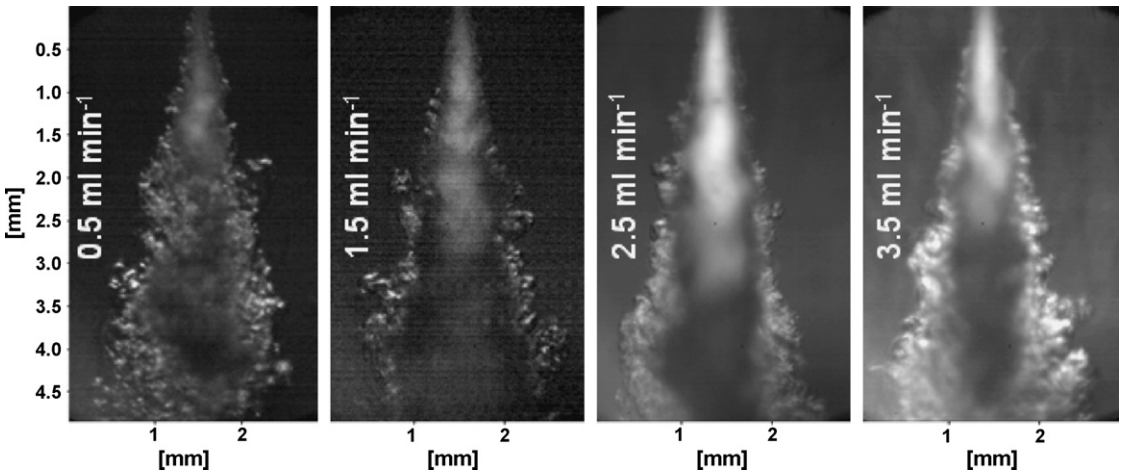

Fig. 11. Light scattering images of DMSO for different flow rates at conditions close to the MCP (10 MPa, 40 °C, ∅ = 80 μm).

complete degradation of the transient interfacial tension between the injected solvent and the bulk CO_2 is longer than the residence time before jet break-up, droplets are formed after jet break-up and Mie scattering signals can be identified. This is the case for all investigated DMSO flow rates at 10 MPa. Further downstream the phase boundaries disappear, as the Mie scattering signals disappear, too. Between the Mie scattering and the Rayleigh scattering signals, a dark region can be identified, from which no signals can be detected. This region is the homogeneous jet core, which is represented by part (d) in Fig. 3. Consequently, under supercritical conditions, closely above the MCP there is a transition within the jet from multi-phase mixing to single-phase mixing. This transition occurs after jet break-up (therefore, droplets are formed), as soon as the transient interfacial tension between the liquid phase and the bulk CO_2 has gone to zero.

Fig. 12 shows the jet behavior at conditions close to the MCP (10 MPa and 40 °C) for different flow rates of acetone and for the nozzle diameter of 80 μm.

The acetone jet characteristics at conditions near above the MCP are very similar to the acetone jet characteristics far above the MCP described in Fig. 10. A jet core, which is described by part (d) in Fig. 3, is visible only for the acetone flow rates exceeding 0.5 mL min^{-1}. For the conditions near above the MCP only gradient scattering signals can be detected for acetone. Increasing the acetone flow rate, the jet core, which is described by part (d) in Fig. 3, is increased. A jet core is not visible for the lowest acetone flow rate. Apparently, for the injection of acetone at 10 MPa, the transient interfacial tension between the injected solvent and the bulk CO_2 is completely zeroed, before jet break-up and no Mie scattering signals are observable. The faster transient interfacial tension degradation of acetone relative to DMSO, must be assigned to the surface tension and the viscosity, which are both smaller for acetone and to the corresponding higher Re numbers and smaller Oh numbers (see Table 1). For example, Re number for acetone is more than fourfold higher for acetone than for DMSO, at the same condition of pressure, nozzle diameter and flow rate.

3.5. Pressure variation at constant flow rate

Fig. 13 shows the jet behavior at different pressures operating at 40 °C and for a DMSO flow rate of 2.5 mL min^{-1} through the 80 μm nozzle.

At 8.5 MPa (at subcritical conditions) a dense droplet laden spray can be identified. Single droplets are not detectable, but intense Mie scattering signals prove their existence. Therefore, jet mixing at 8.5 MPa clearly takes place in a multi-phase flow. At 9.0 MPa, the jet already has characteristics of both, multi-phase mixing in the jet centre with Mie scattering signals and single-phase mixing at the jet edges with Rayleigh scattering signals. Within the jet core, bright Mie scattering signals prove the presence of small

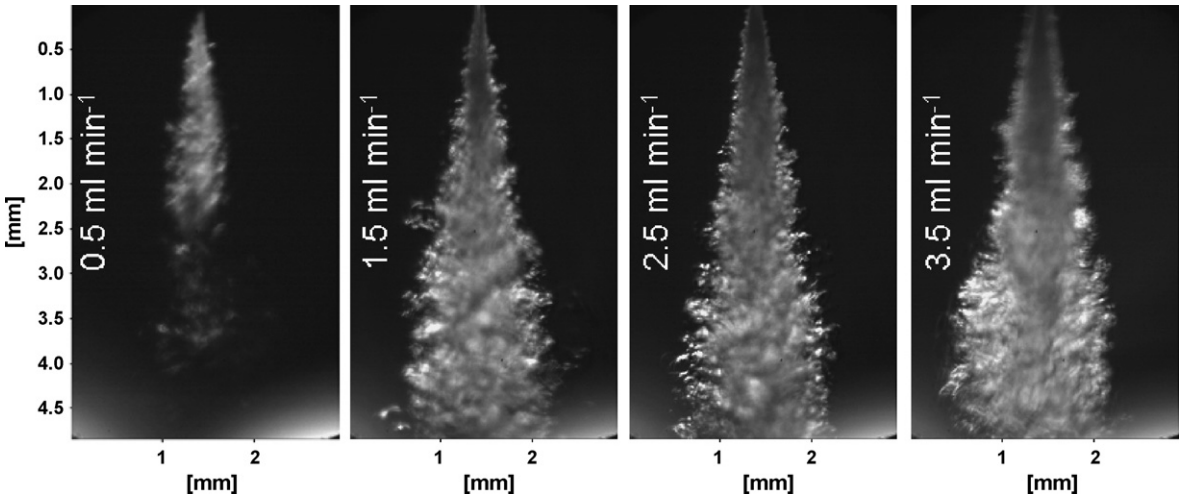

Fig. 12. Light scattering images of acetone for different flow rates at conditions close to the MCP (10 MPa, 40 °C, ∅ = 80 μm).

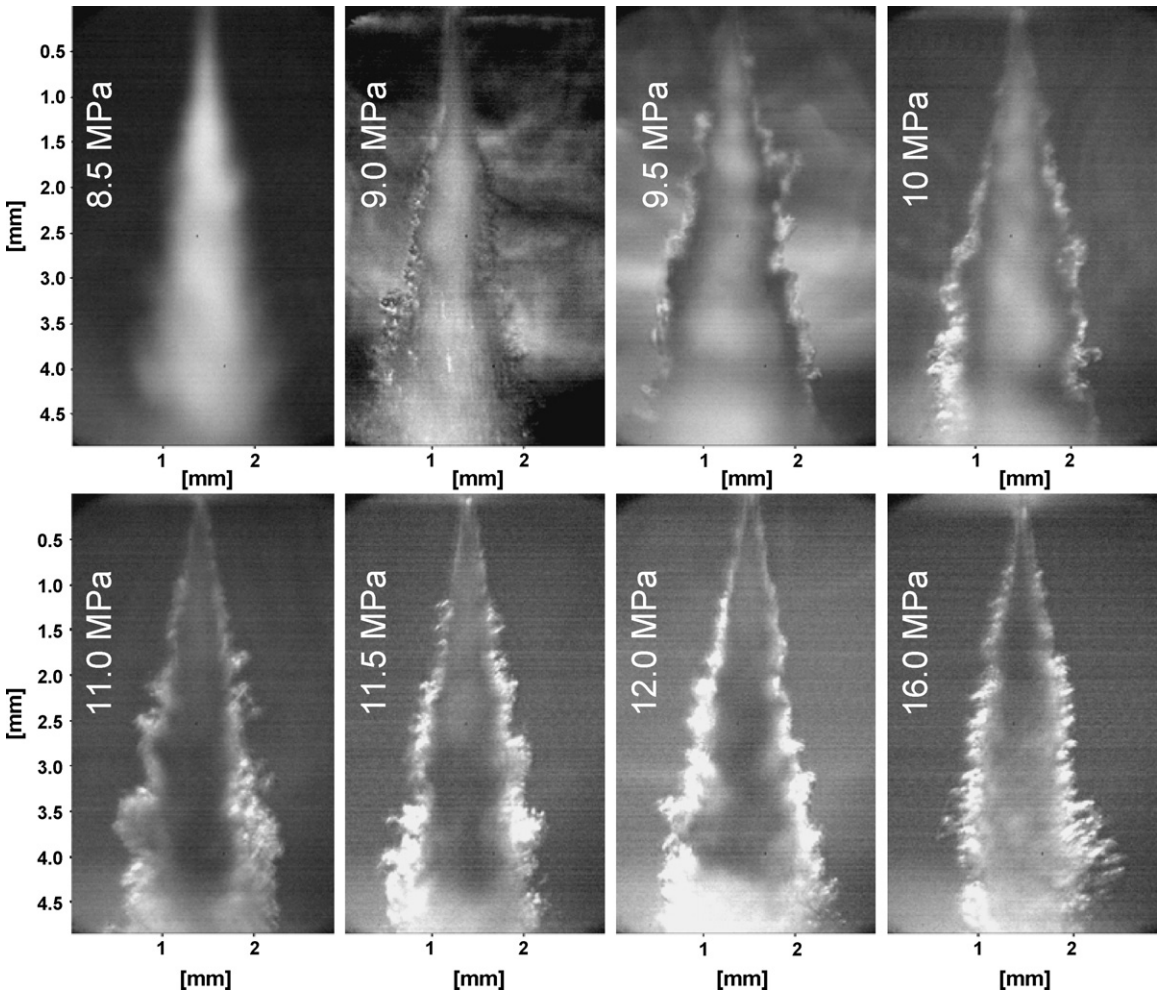

Fig. 13. Light scattering images of DMSO at a constant flow rate of 2.5 mL min^{-1} through a 80 μm diameter injection nozzle for different pressures at 40 °C.

droplets. There is a narrow dark gap between the Mie scattering signals in the jet core and the Rayleigh scattering signals at the jet edges. Increasing the pressure, the dark gap, which indicates the transition from multi-phase to single-phase mixing, enlarges between the jet centre and the jet edges. Up to 12 MPa there is still a Mie scattering signal detectable at the jet centre, in the upper part of the jet images (weak but detectable), due to the presence of droplets. At pressures exceeding 12 MPa, for example, at 16 MPa, the jet consists only of parts (d) and part (e) as described in Fig. 3. Consequently at 16 MPa, jet mixing takes place completely within a homogeneous single phase. This series of images demonstrates that in the case of DMSO at pressures larger than the MCP a progressive transition exists between multi-phase and single-phase mixing. It ends at pressures of approximately 12 MPa. If the same experiments are carried out substituting DMSO with acetone, Mie scattering signals from phase boundaries are detectable only up to a pressure of 8 MPa within the whole jet (corresponding jet images are not given). For higher pressures the jet images are always composed of part (d) and part (e) as described in Fig. 3. The jet core region (part d) becomes shorter with increasing pressure. A transition from multi-phase to single-phase mixing within the jet is not observed, even for pressures very close to the MCP.

3.6. Nozzle diameter variation at constant Reynolds number

Fig. 14 shows light scattering images of DMSO jets for SAS conditions below and above the MCP for the system DMSO/CO_2. The three jet images in the upper line correspond to the injection through the 80 μm nozzle, while the three images in the lower line correspond to the injection through the 160 μm diameter nozzle. To keep the Reynolds number constant for a given pressure but operating with different nozzle diameters, the flow rate was modified as can be extracted from Table 1. Comparing the upper with the lower line in Fig. 14, it becomes evident, that the jet images have the same characteristics. At 8.5 MPa (below the MCP), intense Mie scattering signals prove the existence of a dense droplet laden spray. At 10 MPa the jet images show both Mie scattering signals in the jet centre and Rayleigh scattering signals at the jet edges. For the nozzle diameter of 80 μm there is additionally a transition between the multi-phase and the single-phase mixing area, which is the dark region between the Mie scattering and the gradient scattering signals.

This dark transition area is not observable using the 160 μm diameter nozzle at the same pressure. At 16 MPa the jet image consists of a jet core and an area of pronounced composition gradients (gradient scattering signals), which are described by part (d) and part (e) in Fig. 3, respectively. No transition from multi-phase to single-phase mixing can be identified within jet images. The differences, for example, a more pronounced multi-phase mixing regime for the 160 μm diameter nozzle at 10 MPa, could be assigned to the different flow rates. To keep the Reynolds number constant, according to Eq. (1) the nozzle exit velocity has to be adjusted inversely proportional to the nozzle diameter variation. This result can be obtained, if the flow rate is adjusted in a manner

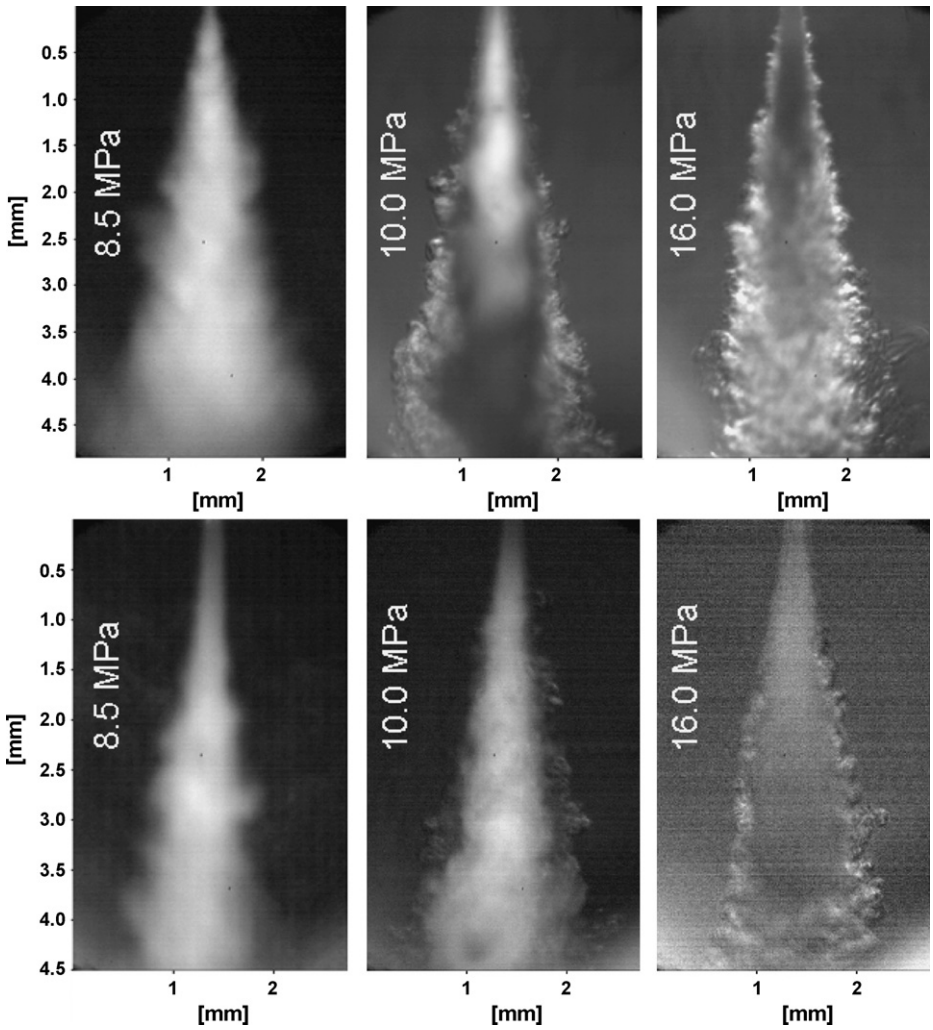

Fig. 14. Light scattering images of a DMSO jet for two different nozzle diameters and three different pressures at 40 °C. The flow rates were adjusted to keep the Reynolds number constant for a constant pressure but different nozzle diameters (upper line: ⌀ = 80 μm, flow rate = 3.5 mL min^{-1}; lower line: ⌀ = 160 μm, flow rate = 7.0 mL min^{-1}).

that is directly proportional to the nozzle diameter variation. Consequently, to assure Reynolds equivalence, the flow rate and the nozzle exit velocity are counter propagating. Thus, for the 160 μm nozzle a high flow rate, but a small nozzle exit velocity is realized in comparison to the 80 μm nozzle, where a smaller flow rate but a higher exit velocity is realized. The smaller nozzle diameter in combination with the higher exit velocity promotes the formation of smaller droplets. Additionally, the overall flow rate penetrating into the bulk CO_2 is smaller than for the 160 μm diameter nozzle. The combination of these effects gives an explanation of the transition region from multi-phase to single-phase mixing observable only for the 80 μm diameter nozzle at 10 MPa. The same considerations explain the differences at the same Reynolds number between jet images at 8.5 and 16 MPa. Nevertheless, the jet characteristics (not the intensity of the jet characteristics), under Reynolds equivalent conditions and at a fixed pressure are not affected by the variation of the nozzle diameter.

3.7. Experiments using a solute

For the correlation of fluid dynamics with particle morphology, a further series of experiments were performed adding YAc to DMSO at solution concentrations ranging between 15 and 50 mg mL^{-1}. As already explained, this compound was previously investigated by SAS and its precipitates showed various useful morphologies like microparticles, nanoparticles and expanded microparticles [3,4,12]. These morphologies are not characteristic of YAc only; but, many other compounds showing the same morphologies are reported in the literature [4], among these: antibiotics, drugs; colouring matters; polymers, explosives, catalysts precursors. Therefore, YAc represents a wide group of compounds studied and these results can be easily extended.

Experiments were performed on the same apparatus as in the previous part of the work and at steady state composition conditions in the precipitator (see Section 2.3). In the first part of the experiment only the mixing behavior of DMSO was monitored and in the second part of the experiments DMSO + YAc with precipitation was investigated. No relevant modifications in the jet fluid dynamics were observed when YAc was added to the solvent. Moreover, a systematic collection of precipitates was performed at the end of each experiment to look for a correlation between the observed fluid dynamic phenomena and particle morphology.

In the experiments performed at pressures below the MCP and at atomization conditions (8.5 MPa, 40 °C, ⌀ = 80 μm, 0.5 mL min^{-1}, concentration 15 mg mL^{-1}) the YAc collected powder is formed by large microparticles. Fig. 15 shows a scanning electron microscopy (SEM) image of a sample of the corresponding particles. Some of them are broken and show to be empty indicating that the so-called expanded microparticles were produced. They are ranging between 3 and 20 μm. The mode obtained by calculating the PSD is 13.7 μm with a standard deviation of 3.2.

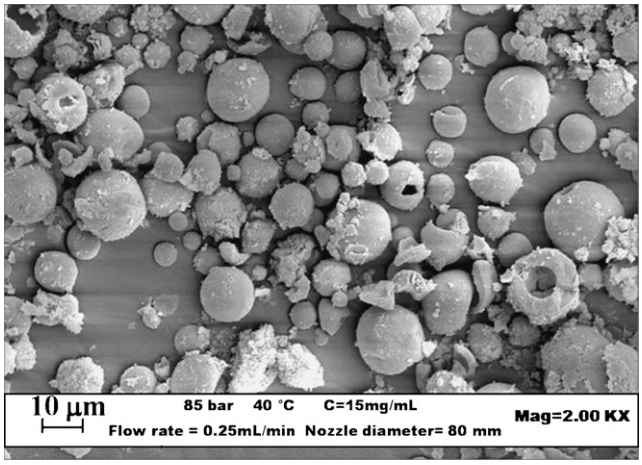

Fig. 15. SEM image of YAc expanded microparticles obtained by SAS at 8.5 MPa and 40 °C with a DMSO flow rate of 0.25 mL min^{-1} through a 80 μm diameter nozzle.

It is also worth to note the fact that the surface of these particles is formed by networked nanoparticles as shown in Fig. 16.

We performed some experiments at SAS operating at conditions for which the transition from multi-phase to single-phase mixing was found within the jet. An example of this kind of obtained particles is shown in Fig. 17. Micrometric spherical particles ranging between 0.5 and 10 μm were generated, and they were observed in the run performed at 12 MPa, 50 mg mL^{-1} YAc in DMSO, a solution flow rate of 0.5 mL min^{-1}, through the 160 μm diameter nozzle. The particles shown in Fig. 17 are almost perfectly spherical and show a continuous surface. The mode obtained by calculating the PSD is 1.2 μm with a standard deviation of 0.8.

When SAS experiments were performed at pressures far above the MCP as previously discussed, a gas-like mixing process was observed and nanoparticles were obtained as irregularly spherical nanoparticles ranging between about 70 and 120 nm. Fig. 18, for example, shows the nanoparticles produced in the experiment performed at 16 MPa, 40 °C, 15 mg mL^{-1} YAc in DMSO and a solution flow rate of 0.5 mL min^{-1} through a 160 μm diameter nozzle. The mode obtained by calculating the PSD is about 90 nm with a standard deviation equal to 25.999

4. Discussion

In this work dripping, jet atomization and gas-like mixing were observed using the light scattering technique, substantially confirming the observations of the authors [7,10,11,14,15] that have previously studied SAS fluid dynamics. Dripping is simply due to the use of liquid flow rates that are too low to produce a continuous liquid flow and do not produce atomization. Jet atomization and gaseous mixing and, particularly their competition at some process conditions require a detailed analysis.

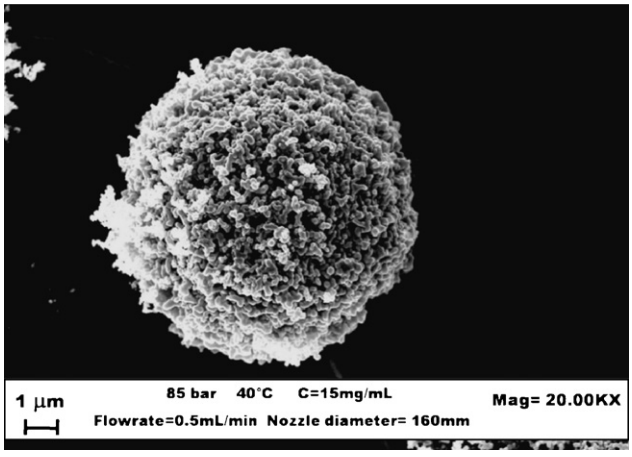

Fig. 16. SEM detail of YAc expanded microparticle obtained operating at the same process conditions as in Fig. 15.

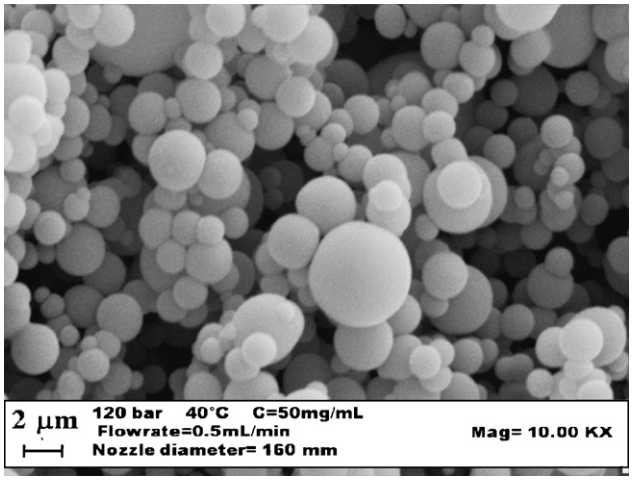

Fig. 17. SEM image of YAc micrometric particles obtained by SAS at 12 MPa, 40 °C, 50 mg mL^{-1} YAc in DMSO and a solution flow rate of 0.5 mL min^{-1} through a 160 μm diameter nozzle.

4.1. Subcritical conditions

Operating at pressures below the MCP, multi-phase mixing was consistently observed for acetone and DMSO. On the contrary, gas mixing has never been observed at these conditions. The explanation of these experimental evidences is that at subcritical conditions the interfacial tension between the injected liquid and the bulk phase never goes to zero and a supercritical mixture is not formed between the liquid solvent and CO_2. The droplets formed during atomization are subjected to a very fast internal formation of a liquid/CO_2 mixture. Due to a high solubility of CO_2 in pressurized organic liquids and a very poor evaporation of organic solvents into the bulk CO_2, the droplets expand. During these processes, the interfacial tension allows the droplets to maintain its spherical shape, even when the solute is precipitated within the

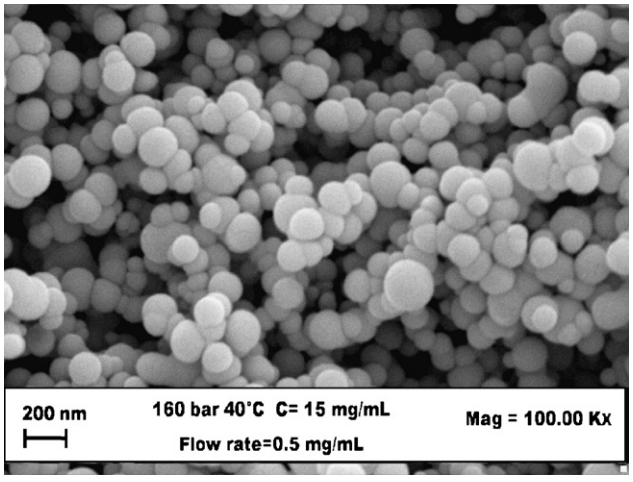

Fig. 18. SEM image of YAc nanoparticles obtained by SAS far above the MCP: 16 MPa, 40 °C, 15 mg mL^{-1} YAc in DMSO and a solution flow rate of 0.5 mL min^{-1} through a 160 μm diameter nozzle.

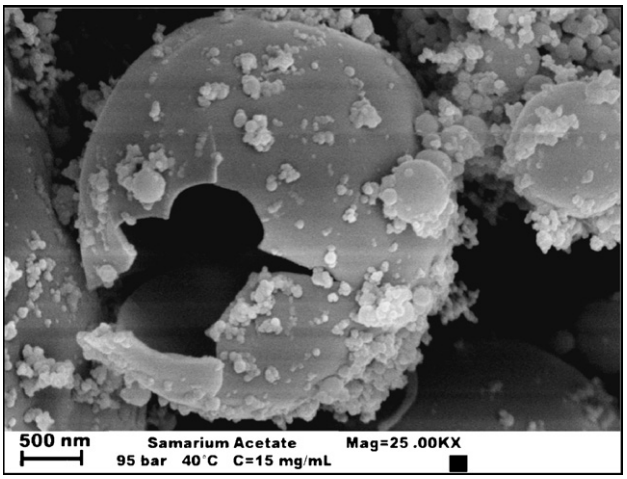

Fig. 19. SEM image detail of an expanded samarium acetate hollow microparticle, characterized by a smooth surface [12].

droplet. Saturation occurs at the droplet surface and solidification takes place with all solutes progressively condensing on the particle internal surface. The final result is the formation of a solid shell. This result is well illustrated in Fig. 16 for YAc. This kind of particles has also been observed in other SAS works [12]. For example, an expanded hollow particle of samarium acetate, reported in Fig. 19, has been obtained by SAS precipitation from DMSO, operating at 9.5 MPa, 40 °C, and with a concentration of 15 mg mL^{-1} samarium acetate. In this case a continuous shell surface is evidenced.

The two different surface morphologies can depend on different controlling mass transfer mechanisms, as suggested by Duhkin et al. [9]: diffusion controlled solidification of the particle can produce a continuous surface; nucleation controlled solidification can produce the simultaneous formation of many nuclei at different locations within the droplet and can induce the formation of connected nanoelements even on the surface of the microparticle (Fig. 16).

4.2. Near above the MCP

Operating conditions above the MCP, from a thermodynamic point of view, are characterized by zero interfacial tension. But, the liquid injected into the precipitator, before equilibrium conditions are obtained, experiences the transition from a pure liquid to a supercritical mixture. Therefore, interfacial tension starts from the value typical of the pure liquid and progressively reduces to zero. This fact means that droplets formed after jet break-up (whose presence indicates in every case the existence of an interfacial tension) are formed before the disappearance of the interfacial tension. In other words, the time of equilibration (obtainment of the thermodynamic conditions) is longer than the time of jet break-up. After the droplet is formed, surface tension continues to reduce until it completely disappears. Therefore, the droplets do not sensibly expand as at subcritical conditions. For this reason, when a solute is present, it precipitates collapsing in the whole volume occupied by the liquid and non-hollow particles are formed as shown in Fig. 17.

Another observation should be made about the dimensions of the droplets and consequently of the particles that are formed operating at these conditions. As reported in Fig. 17, the particles diameter ranges between about 0.5 and 10 μm, though the nozzle diameter was 160 μm and the solution flow rate was 0.5 mL min^{-1}. For mild injection conditions like these, the formation of rather large drops or droplets is expected for classical spray approaches. Nevertheless, as can be seen from Fig. 11 the intense Mie scattering signals prove the existence of very small droplets. This observation means that the SAS atomization is extremely efficient. Indeed, as shown in Lefevre [30], the mean droplets size for a classical atomization using similar nozzle diameters should measure about a tenth of microns. A possible explanation for the extreme efficient atomization into small droplets is again the reduced interfacial tension at which the droplets are generated. As expected, an increase of YAc concentration in the starting solution produced an increase of the particle size that is correlated to liquid droplets dimensions, i.e., larger droplets are produced by an increase of the solution viscosity and consequently larger particles are collected. The comparison of the mixing behavior of acetone and DMSO in CO_2 at pressures slightly above their respective MCP evidences that DMSO jets show the characteristics of multi-phase mixing even at pressures largely exceeding the MCP. For acetone, even at pressures very close above the MCP only single-phase mixing could be identified. The presence of a transient interfacial tension was first introduced in [32] and then proposed by other authors [10] to explain the progressive transition between multi- and single-phase mixing at pressures above the MCP. The different mixing behaviors of DMSO and acetone, as already explained in Section 3.4 can be attributed to the different solvent properties, as summarized in Table 2. It means that the vanishing of the interfacial tension for DMSO requires a longer time than for acetone. Due to the competition between the complete disappearance of the interfacial tension and the jet break-up, multi-phase mixing can prevail at higher pressures for DMSO with respect to acetone.

4.3. Far above the MCP

For pressures far above the MCP single-phase mixing is the only fluid dynamic behavior observed for DMSO and acetone. Again the injected liquid experiences the progressive disappearance of the interfacial tension; but in this case droplets are not formed as the interfacial tension reduces to zero before jet break-up for both solvents. This behavior was observed for acetone already at pressures close above the MCP. At single-phase mixing conditions, solidification of the solute has to be attributed to the classical gas-to-particle nucleation and the subsequent growth mechanism. Gas-to-solid particle formation is, as a rule, characterized by nucleation followed by a reduced growth since mass transfer from the bulk of the gas phase to the surface of the particle is poor, as the solute is practically not soluble in the fluid phase.

5. Conclusions

An overall interpretation of the results reported in this work is possible if they are referred to characteristic time scales:

- (τ_i) for the complete disappearance of the interfacial tension between the injected solution and
- (τ_{jb}) for the time of the jet break-up.

Therefore, it is possible to propose a classification of the observations obtained in this work.

At operation conditions below the MCP, the interfacial tension persists and a multi-phase mixing system results after jet break-up into droplets. At operation conditions above the MCP, the operating conditions and the solvent properties influence τ_i and τ_{jb}. When τ_i is shorter than τ_{jb}, a single-phase mixing system will be formed after jet break-up and nanoparticles are formed due to nucleation mechanisms similar to those of nucleation in a gas phase. If τ_{jb} is shorter, a multi-phase mixing system is generated after jet break-up, which will change to a single-phase mixing system, as soon as the residence time of the injected solution equals τ_i. In this

case it depends on the nucleation kinetics, if precipitation takes place in the multi-phase jet region with the generation of spherical microparticles or in the single-phase jet region with the formation of nanoparticles. The competition of these two timescales also explains why in some cases the coexistence of nanoparticles and microparticles was observed in SEM images of the precipitates. When acetone was used as the solvent above the MCP, the competition between τ_i and τ_{jb} was always won by τ_i, as only single-phase mixing characteristics could be detected. This may be the reason why – to the best of the authors' knowledge – the production of spherical microparticles has never been reported in SAS literature, when acetone was used as solvent.

Summarizing:

- The morphologies observed have been frequently reported in SAS literature, repeated in this work and correlated to the different fluid dynamic regimes.
- The explanation of the mechanisms involved in particle precipitation, is in agreement with the high-pressure phase equilibria and the mass transfer mechanisms. Looking at the results illustrated in the first part of this work they are also in agreement with multi-phase vs. single-phase mixture formation for the liquid injected into the precipitator.
- Expanded spherical particle and spherical microparticle formation depends on droplet formation via jet break-up at subcritical and near supercritical conditions, respectively.
- No droplets are formed at far above MCP supercritical conditions, since the formation of a single-phase mixing system proceeds after the jet break-up. Therefore, precipitation is a gas-to-particle formation process and nanoparticles are produced.
- When τ_i and τ_{jb} are very similar a transition from multi-phase to single-phase mixing within the jet is observed.
- For the first time it has been demonstrated how phase equilibria, jet mixing, and mass transfer interactions influence the complex morphology of the particles observed for YAc and the compound with similar behavior as classified in Ref. [3].
- Other precipitate morphologies that have also been frequently observed in SAS processing have not been considered in this work: mainly crystals with various habits and size have been produced [3]. However, the control of the size and the PSD of these crystals is problematic. It is in the author's opinion that they are produced by a liquid-like behavior that could be characteristic of the SAS operation inside the miscibility hole of the binary solvent–antisolvent, modified by the presence of small quantities of dissolved solute.

Acknowledgments

The authors gratefully acknowledge financial support for parts of this work by the German Research Foundation (DFG) which additionally funds the Erlangen Graduate School in Advanced Optical Technologies (SAOT) in the framework of the German excellence initiative.

References

[1] A. Shariati, C.J. Peters, Recent developments in particle design using supercritical fluids, Curr. Opin. Solid State Mater. Sci. 7 (2003) 371–383.
[2] E. Reverchon, R. Adami, Nanomaterials and supercritical fluids, J. Supercrit. Fluids 37 (2006) 1–22.
[3] E. Reverchon, R. Adami, G. Caputo, I. De Marco, Spherical microparticles production by supercritical antisolvent precipitation: interpretation of results, J. Supercrit. Fluids 47 (2008) 70–84.
[4] E. Reverchon, I. De Marco, E. Torino, Nanoparticles production by supercritical antisolvent precipitation: a general interpretation, J. Supercrit. Fluids 43 (2007) 126–138.
[5] E. Reverchon, G. Caputo, S. Correra, P. Cesti, Synthesis of titanium hydroxide nanoparticles in supercritical carbon dioxide on the pilot scale, J. Supercrit. Fluids 26 (2003) 253–261.
[6] E. Reverchon, I. De Marco, G. Caputo, G. Della Porta, Pilot scale micronization of amoxicillin by supercritical antisolvent precipitation, J. Supercrit. Fluids 26 (2003) 1–7.
[7] E. Badens, O. Boutin, G. Charbit, Laminar jet dispersion and jet atomization in pressurized carbon dioxide, J. Supercrit. Fluids 36 (2005) 81–90.
[8] S. Dowy, A. Braeuer, K. Reinhold-Lopez, A. Leipertz, Laser analyses of mixture formation and the influence of solute on particle precipitation in the SAS process, J. Supercrit. Fluids 50 (2009) 265–275.
[9] S.S. Dukhin, Y. Shen, R. Dave, R. Pfeffer, Droplet mass transfer, intradroplet nucleation and submicron particle production in two-phase flow of solvent–supercritical antisolvent emulsion, Colloid Surf. A 261 (2005) 163–176.
[10] A. Gokhale, B. Khusid, R.N. Dave, R. Pfeffer, Effect of solvent strength and operating pressure on the formation of submicrometer polymer particles in supercritical microjets, J. Supercrit. Fluids 43 (2007).
[11] C.S. Lengsfeld, J.P. Delplanque, V.H. Barocas, T.W. Randolph, Mechanism governing microparticle morphology during precipitation by a compressed antisolvent: atomization vs. nucleation and growth, J. Phys. Chem. B 104 (2000) 2725–2735.
[12] E. Reverchon, I. De Marco, R. Adami, G. Caputo, Expanded micro-particles by supercritical antisolvent precipitation: interpretation of results, J. Supercrit. Fluids 44 (2008) 98–108.
[13] S.-C. Chang, M.-J. Lee, H.-M. Lin, Role of phase behavior in micronization of lysozyme via a supercritical anti-solvent process, Chem. Eng. J. 139 (2008) 416–425.
[14] M. Sarkari, I. Darrat, B.L. Knutson, Generation of microparticles using CO_2 and CO_2-philic antisolvents, AICHE J. 46 (2000) 1850–1859.
[15] D.L. Obrzut, P.W. Bell, C.B. Roberts, S.R. Duke, Effect of process conditions on the spray characteristics of a PLA plus methylene chloride solution in the supercritical antisolvent precipitation process, J. Supercrit. Fluids 42 (2007) 299–309.
[16] S.S. Dukhin, C. Zhu, R. Dave, R. Pfeffer, J.J. Luo, F. Chavez, Y. Shen, Dynamic interfacial tension near critical point of a solvent–antisolvent mixture and laminar jet stabilization, Colloid Surf. A: Physicochem. Eng. Asp. 229 (2003) 181–199.
[17] L.Y. Lee, L.K. Lim, J. Hua, C.-H. Wang, Jet breakup and droplet formation in near-critical regime of carbon dioxide–dichloromethane system, Chem. Eng. Sci. 63 (2008) 3366–3378.
[18] T.W. Randolph, A.D. Randolph, M. Mebes, S. Yeung, Sub-micrometer-sized biodegradable particles of poly(l-lactic acid) via the gas antisolvent spray precipitation process, Biotechnol. Prog. 9 (1993) 429–435.
[19] E. Reverchon, G. Della Porta, I. De Rosa, P. Subra, D. Letourneur, Supercritical antisolvent micronization of some biopolymers, J. Supercrit. Fluids 18 (2000) 239–245.
[20] J.O. Werling, P.G. Debenedetti, Numerical modeling of mass transfer in the supercritical antisolvent process, J. Supercrit. Fluids 16 (1999) 167–181.
[21] J.O. Werling, P.G. Debenedetti, Numerical modeling of mass transfer in the supercritical antisolvent process: miscible conditions, J. Supercrit. Fluids 18 (2000) 11–24.
[22] F. Chavez, P.G. Debenedetti, J.J. Luo, R.N. Dave, R. Pfeffer, Estimation of the characteristic time scales in the supercritical antisolvent process, Ind. Eng. Chem. Res. 42 (2003) 3156–3162.
[23] R. Adami, L.S. Osséo, R. Huopalahti, E. Reverchon, Supercritical antisolvent micronization of PVA by semi-continuous and batch processing, J. Supercrit. Fluids 42 (2007) 288–298.
[24] S. Dowy, A. Braeuer, R. Schatz, E. Schluecker, A. Leipertz, CO_2 partial density distribution during high-pressure mixing with ethanol in the supercritical antisolvent process, J. Supercrit. Fluids 48 (2009) 195–202.
[25] A. Kordikowski, A.P. Schenk, R.M. Van Nielen, C.J. Peters, Volume expansions and vapor–liquid equilibria of binary mixtures of a variety of polar solvents and certain near-critical solvents, J. Supercrit. Fluids 8 (1995) 205–216.
[26] Y. Sun, B.Y. Shekunov, Surface tension of ethanol in supercritical CO_2, J. Supercrit. Fluids 23 (2003) 73–83.
[27] E. Reverchon, G.D. Porta, A.D. Trolio, S. Pace, Supercritical antisolvent precipitation of nanoparticles of superconductor precursors, Ind. Eng. Chem. Res. 37 (1998) 952–958.
[28] A.E. Andreatta, L.J. Florusse, S.B. Bottini, C.J. Peters, Phase equilibria of dimethyl sulfoxide (DMSO) + carbon dioxide, and DMSO + carbon dioxide+water mixtures, J. Supercrit. Fluids 42 (2007) 60–68.
[29] C.-Y. Day, C.J. Chang, C.-Y. Chen, Phase equilibrium of ethanol + CO_2 and acetone + CO_2 at elevated pressures, J. Chem. Eng. Data 41 (1996) 839–843.
[30] A.H. Lefebvre, Atomization and Sprays, Taylor & Franzis, 1989.
[31] O. Ciocirlan, O. Iulian, Vapor pressure, density, viscosity and refractive index of dimethyl sulfoxide + 1,4-dimethylbenzene system, J. Serb. Chem. Soc. 73 (2008) 73–85.
[32] D.D. Joseph, Y.Y. Renardy, Drops and Miscible Fluids, Fundamentals of Two-Fluid Dynamics. Part II. Lubricated Transport, Springer, New York, 1992.